Measurement of Ionospheric TEC in Spaceborne SAR Data

Michael Jehle, *Student Member, IEEE*, Othmar Frey, *Member, IEEE*, David Small, *Member, IEEE*, and Erich Meier, *Member, IEEE*

***Abstract*—The propagation of spaceborne radar signals operating at L-band frequency or below can be seriously affected by the ionosphere. At high states of solar activity, Faraday rotation (FR) and signal path delays disturb radar polarimetry and reduce resolution in range and azimuth. While these effects are negligible at X-band, FR and the frequency-dependent path delays can become seriously problematic starting at L-band. For quality assurance and calibration purposes, existing L-band or potential spaceborne P-band missions require the estimation of the ionospheric state before or during the data take. This paper introduces two approaches for measuring the ionospheric total electron content (TEC) from single-polarized spaceborne SAR data. The two methods are demonstrated using simulations. Both methods leverage knowledge of the frequency-dependent path delay through the ionosphere: The first estimates TEC from the phase error of the filter mismatch, while the second gauges path-delay differences between up and down chirps. FR, mean (direct current) offsets, and noise contributions are also considered in the simulations. Finally, possibilities for further methodological improvements are discussed.**

***Index Terms*—Advanced Land Observing Satellite Phased Array L-band Synthetic Aperture Radar (PALSAR), ionosphere, SAR processing, synthetic aperture radar (SAR), total electron content (TEC).**

I. Introduction

A MAJOR problem in assessing the global carbon cycle is the state of understanding of the terrestrial ecosystem. Measuring the biomass on a global scale including its temporal variations would help to improve the knowledge of these processes. Good estimates of forest biomass could be obtained from synthetic aperture radar (SAR) at lower frequencies such as P-band [1]. However, the performance of a spaceborne SAR system at lower frequencies is often significantly degraded by the effects of the ionosphere. In order to correct or avoid these problems, it is necessary to assess the ionospheric state before or during a data take.

Under strong solar activity, the influence of the ionosphere on radar-signal propagation at L- and P-bands becomes a significant error source. Low frequencies and high chirp-signal bandwidth are more susceptible to effects like signal path delay and Faraday rotation (FR). Frequency-dependent path delays and FR result in changes to the chirp length and imply a variation of the chirp amplitude for single-polarized sensor configurations. While these effects are not noticeable at X-band frequencies and above, the performance of sensors starting at L-band and lower is reduced [2].

Since the launch of the Advanced Land Observing Satellite and the onboard Phased Array L-band SAR (PALSAR) instrument, spaceborne SAR data at L-band have been available to study the ionospheric effects from polarimetric measurements. Depending on the acquisition mode, the PALSAR range chirp bandwidth can be as high as 28 MHz. A preliminary study investigated the influence of the ionosphere at low frequencies (L-band and lower). Signal degradation caused by the ionosphere also increases with larger chirp bandwidths [3], [4].

In this paper, the aim is to describe algorithms and possibilities for the estimation of the ionospheric total electron content (TEC) from low-carrier-frequency high-bandwidth SAR raw data. The chirp replica is iteratively modeled until it best matches a synthetic pulse deformed under the influence of the ionosphere. In a second approach introduced later, the phase information from alternating up and down chirps is utilized. Changes causing phase advance, chirp-length modification, and amplitude and chirp-rate modulations are considered to evaluate local TEC levels.

The potential of low-frequency SAR with ionospheric path delays and FR for TEC measurements was recognized in [2] and [5]. FR effects were discussed at length in [6]–[8]. Corrective methods were treated in [9], and distortion effects were discussed in [10]. Detection and estimation techniques based on quad-polarized data are presented in [6] and [11]–[13]. A good estimation improves general polarimetric calibration and validation techniques such as those described in [14] and [15], helping to improve the reliability of spaceborne polarimetric measurements for biomass classification and retrieval [16], [17]. In [18] and [19], a first analysis of PALSAR data considering FR detection was presented. An alternative concept for spaceborne SAR at low frequencies was shown in [20].

In Section II, the theoretical background of the ionospheric influences on electromagnetic waves is outlined. The algorithms used for the simulation of spaceborne SAR backscatter from a trihedral corner reflector (TCR) are introduced (including FR). The influence of the frequency-dependent path delay within a radar up or down chirp is explained and integrated in the simulation. Simulations are then carried out for typical L- and P-band sensor configurations with multiple targets in a scene.

To estimate TEC levels from SAR raw data, two methods are described in Sections III and IV. The suitability of SAR

Manuscript received May 28, 2009; revised October 7, 2009. Date of publication March 8, 2010; date of current version May 19, 2010. This work was supported by the European Space Agency under Contract 20046/06/NL/CO.

The authors are with the Remote Sensing Laboratories, Department of Geography, University of Zurich, 8057 Zürich, Switzerland (e-mail: michael.jehle@geo.uzh.ch; othmar.frey@geo.uzh.ch; david.small@geo.uzh.ch; erich.meier@geo.uzh.ch).

Digital Object Identifier 10.1109/TGRS.2010.2040621

data to TEC estimation under real conditions is assessed using comparable noise levels, FR, and disturbing targets within a scene. The results of simulated L- and P-band data are compared, and possible methods for proper validation are suggested. In conclusion, the results are summarized in Section V, and directions for further research are discussed.

II. Effects of the Ionosphere

Electromagnetic waves propagating through the ionosphere experience a polarization rotation of the electric field vector and a signal path delay that depends on the free electron density number N_e along the ray path, the signal frequency f, and the strength of the magnetic field parallel to the propagation direction of the wave within the ionized layer. The reversal of paths in two-way propagation from a satellite to the Earth and back does *not* compensate for this effect. Instead, the effect is cumulative: FR *doubles* as does the path delay [3].

A. Ionosphere

In a manner similar to chromatic aberration in a camera lens, wavelength-dependent distortions can be introduced to radar measurements by the ionosphere. Spaceborne SAR systems usually transmit linear frequency-modulated chirp pulses. Mathematically, a chirped pulse s_0 is a function of time t and can be written as

$$s_0(t) = U_{\mathrm{st}} \cdot e^{j2\pi(f_{\mathrm{start}} \cdot t \pm \alpha \cdot t^2)} \qquad 0 \le t \le T_p \tag{1}$$

where the amplitude U_{st}, the start frequency of the chirp $f_{\mathrm{start}} = f_c \pm f_0$, the chirp rate $\alpha = f_0/T_p$, and the pulse duration T_p parameterize the chirps. f_c is the center frequency, and $f_0 = B/2$ is half of the chirp bandwidth B. The $\pm$ distinguishes between up and down chirps. As the refractive index of the ionosphere is dependent on frequency, each sample of a chirp is delayed individually. The *group* refractive index of the ionosphere can be estimated from

$$n \approx 1 + \frac{f_N^2}{2f^2} \tag{2}$$

$$f_N^2 = \frac{N_e e^2}{4\pi^2 \varepsilon_0 m_e} = 80.56 N_e \tag{3}$$

where f_N is the plasma frequency, e is the charge of an electron, m_e is the electron mass, and ε_0 is the electric permittivity. The delay by the ionosphere compared with vacuum conditions is given by

$$\Delta t = \frac{1}{c} \int\limits_{\mathrm{path}} n - 1 \, ds = \frac{40.28}{cf^2} \int\limits_{\mathrm{path}} N_e \, ds = \frac{40.28}{cf^2} \mathrm{TEC}. \tag{4}$$

Based on the individual path delays at either end of the chirps, a modified chirp rate and pulse duration can be estimated to simulate the chirp after propagation through the ionosphere. The matched filtering of the chirp was done by the convolution of the measured signal s_r with the complex conjugate of the transmitted chirp s_t^*. For the range-compressed signal s_{rg}, one has

$$\begin{aligned} s_{\mathrm{rg}} &= s_t^*(t) * s_r(t) \\ &= \mathcal{F}^{-1}\left\{S_t(w)^* \cdot S_r(w)\right\} \end{aligned} \tag{5}$$

where $S_t(w)$ and $S_r(w)$ are the Fourier transforms of s_t and s_r, respectively, and $\mathcal{F}^{-1}$ denotes the inverse Fourier transform.

B. FR

At L-band frequencies or lower, FR has serious effects on SAR imagery. Backscatter measurements from single-polarized sensor configurations can become ambiguous at high-solar-activity conditions. Within the following simulations, FR is expected to play a minor role as there is only a small change in polarization rotation *within* a chirp. Nevertheless, FR rotation was considered in the simulations. The one-way FR Ω may be estimated from [7] and [9] as

$$\begin{aligned} \Omega &= \frac{2.365 \cdot 10^4}{c^2} \cdot \lambda^2 \cdot B_{\parallel} \int\limits_0^h N_e \, dh \\ &\approx \frac{2.365 \cdot 10^4}{f^2} \cdot \mathrm{VTEC} \cdot \frac{1}{\cos\gamma} \cdot B_{\parallel} \end{aligned} \tag{6}$$

where $B_{\parallel}$ is the mean parallel magnetic field within the ionized layer, λ is the wavelength of the radar wave, VTEC is the vertical TEC (TEC in nadir direction), and γ is the off-nadir angle of observation. The factor $1/\cos\gamma$ is used to transform the vertical electron content to the electron content along the propagation path h. The commonly used zenith angle of the radar wave at the subionospheric point was therefore approximated by the satellite's off-nadir angle [21]. VTEC may be estimated using global ionospheric maps from the Center for Orbit Determination in Europe [22]. γ may be obtained for each image location in a product from the sensor data annotations for most current SAR satellites. The parallel magnetic field was estimated using the International Geomagnetic Reference Field model (IGRF10) [23]. More details on the modeling of FR can be found in [13].

C. Chirp-Signal Path Delay

Within the ionospheric layer, the refractive index that the wave group sees increases at higher solar activity to above unity. As information within a radar pulse travels with the group velocity, the arrival of the pulse back at the antenna is delayed according to [24] and (4) by

$$\Delta t_{\mathrm{iono}} = 2 \cdot \frac{K}{c} \cdot \frac{\mathrm{TEC}}{f^2} \tag{7}$$

where c is the speed of light, TEC is the TEC along the signal path, and $K = 40.28\ \mathrm{m^3/s^2}$ is a refractive constant. For two-way propagation from a satellite to the Earth and back, the pulse front is delayed between

$$t_{\mathrm{shift\_min\_}d} = 2 \cdot \frac{K}{c} \cdot \frac{\mathrm{TEC}}{(f_c + f_0)^2} \tag{8}$$

$$t_{\mathrm{shift\_min\_}u} = 2 \cdot \frac{K}{c} \cdot \frac{\mathrm{TEC}}{(f_c - f_0)^2} \tag{9}$$

where the indexes d and u indicate that the starting frequency of the up or down chirp is used, respectively. The new pulse

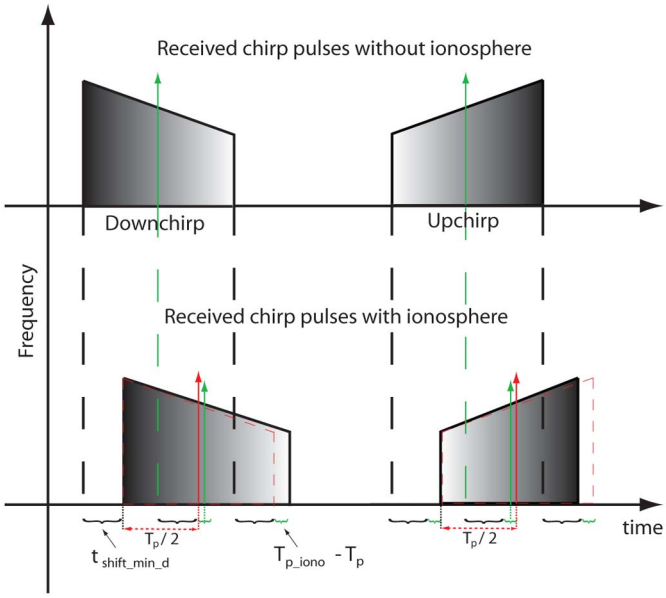

Fig. 1. Received chirp pulses (top) without and (bottom) including ionospheric effects. The green arrows show where the pulses center after range compression. (Red dashed line) Shape of transmitted chirp aligned to received pulse. (Red arrow) Peak after range compression matched to the transmitted pulse.

duration of the chirp after traversing the ionosphere twice can be calculated as

$$T_{p\_\mathrm{iono}} = T_p \mp \frac{2}{c} \cdot K \cdot \mathrm{TEC} \cdot \left(\frac{1}{(f_c - f_0)^2} - \frac{1}{(f_c + f_0)^2} \right). \tag{10}$$

The time delay of the pulse and the accompanying linear chirp-rate alterations imply also phase distortions. Given that the frequency components are invariant under nonneutral (vacuum) ionospheric conditions, there must be a phase advance approximately equal to the path delay. The refractive index for the phase is reduced to less than unity. The extent of the phase advance can therefore be estimated using the time delay Δt_{iono} together with the angular frequency $\omega = 2\pi f$

$$\Delta\phi = -\omega \cdot \Delta t_{\mathrm{iono}} = -\frac{4\pi \cdot 40.28}{cf} \cdot \mathrm{TEC}. \tag{11}$$

For a linearly frequency-modulated chirp, these frequency-dependent shifts imply a slight change in the chirp rate and, thus, a change in the length of the received pulse. Fig. 1 shows a sketch of the expected chirp-path and chirp-length variations caused by the ionosphere. The pulses at the top sketch the shape of down and up chirps under neutral ionospheric conditions. The green arrows mark where the pulses center after range compression. The pulses at the bottom are simulated for an ionized state of the ionosphere. The red dashed line shows the shape of the transmitted pulse aligned to the left with the received pulse to outline the chirp-length and chirp-rate variations before and after passing through the ionosphere. The green arrows again show where the pulses center after matched filtering when using a reference chirp similar to the transmitted chirp. Matching the received signals with the unaltered transmitted pulses causes a slight filter mismatch and, therefore, a marginally shorter arrow length. The red arrows show where the pulses would center if the ionosphere were absent with a constant path delay applied, shifting the dashed red pulse before the deformed pulses.

The most crucial parameter in the matched-filtering process is the chirp rate. A varying chirp rate causes a filter mismatch if left uncorrected, broadening the main lobe and raising the sidelobes. A parameter that is a measure for the broadening of the pulse is the quadratic phase error (QPE). The QPE at the margins of a chirp with pulse duration T_p can be estimated for a signal at baseband from the phase difference of the signals at the time $T_p/2$ using [25]

$$\begin{aligned} QPE &= \phi\left(s_t\left(\frac{T_p}{2}\right)\right) - \phi\left(s_r\left(\frac{T_p}{2}\right)\right) \\ &= 2\pi\Delta\alpha \cdot \left(\frac{T_p}{2}\right)^2 \\ &= 2\pi f_0 \left(\frac{1}{T_p} - \frac{1}{T_{p\_\mathrm{iono}}}\right) \cdot \left(\frac{T_p}{2}\right)^2 \\ &= \frac{4\pi K f_0 T_p}{cT_{p\_\mathrm{iono}}} \frac{f_c f_0}{(f_c - f_0)^2 (f_c + f_0)^2} \cdot \mathrm{TEC} \\ &\approx \frac{4\pi K f_0^2}{cf_c^3} \cdot \mathrm{TEC} \end{aligned} \tag{12}$$

where the indices t and r mark the transmitted or received pulse, respectively, and $\Delta\alpha$ is the change in the chirp rate. The phase error at the peak of the range-compressed target is found to be $QPE_{\mathrm{peak}} \approx QPE/3$[25]. The unequal length of the matched pulses shifts the range-compressed peak by half of the chirp-length difference, causing an additional phase shift equal in magnitude to the QPE when compared to an ideal matched-filtering result. CPE denotes the third-order phase error as it can be estimated using the Taylor series expansion of the ionospheric transfer function [26]. As their contribution is in the range of a hundredth of a degree, it can safely be neglected in the simulations.

III. Simulations

The simulation of ionospheric effects in SAR data enables the testing of new methodologies to estimate the ionospheric state during a SAR acquisition. Ionospheric states can be modeled and tested under consistent geometric conditions and without any temporal decorrelation. When simulating the influence of TEC on SAR signals, the bandwidth-dependent ionospheric behavior described previously must be considered. In the following simulations, the modifications caused by the ionosphere are incorporated by replacing the reference chirp rate and the time-delay vector with values corresponding to a modeled ionospheric state, enabling the simulation of frequency-dependent FR. The signal return of TCRs under typical noise levels and including direct-current (dc) offsets is analyzed. Possibilities for estimating the traversed TEC from the analysis of the modified chirp or the phase difference of an alternating pair of chirps are evaluated. The PALSAR instrument (L-band) and a possible P-band configuration for a spaceborne sensor parameterize the simulations. The configuration parameters are

TABLE I
SAR SYSTEM CONFIGURATION DETAILS AND EXPECTED IONOSPHERIC EFFECTS AT NADIR BASED ON SIMULATIONS

Sensor	**L-band** PALSAR FBS			**P-band** ESA Biomass		
Frequency (f_c) [GHz]	1.27			0.435		
Bandwidth (B) [MHz]	28			6		
Chirp duration [μsec]	27			27		
Sampling rate [MHz]	32			8		
Chirp form	down			down		
Orbit (altitude) [km]	695			695		
TEC [TECU]	**5**	**15**	**25**	**5**	**15**	**25**
Path delay (2-way) at f_c [m]	2.50	7.49	12.48	21.3	63.9	106.4
Change in chirp length (2-way) over B [m]	0.11	0.33	0.55	0.59	1.76	2.93
Faraday rotation at f_c (2-way) [°]	2.95	8.86	14.8	25.2	75.5	125.9
QPE and CPE at $\frac{T_p}{2}$ (2-way) [°]	0.46 0.01	1.39 0.02	2.31 0.03	0.53 0.00	1.58 0.01	2.64 0.02
Phase error at RC peak (2-way) [°]	0.62	1.85	3.09	0.71	2.11	3.52

listed in Table I together with the corresponding typical effects on the pulse at different ionospheric states. Significantly higher TEC values are expected in the equatorial region at solar max.

A. TEC Autofocus

The estimation of TEC from SAR data by evaluating pulse degradation requires high contrast, typically strong point targets such as corner reflectors within an otherwise dark area, to achieve a high signal-to-clutter ratio (SCR).

One models ionospheric states differing from neutral ionospheric conditions (vacuum) to an ionized state where both pulses match optimally. The algorithm iteratively tries to compensate the phase error caused by a change in the chirp rate of the pulse while propagating through the ionosphere and is comparable to existing SAR azimuth autofocusing techniques such as the phase gradient or the range Doppler algorithm [25], [27].

A chirp replica is built using the static system parameters such as chirp bandwidth, chirp form (up or down chirp), pulse repetition frequency (PRF), sampling rate, and center frequency. As the TEC level is successively increased, the chirp rate of the reference pulse is modified. Range compression is then done repeatedly with a set of generated TEC-dependent reference chirps. As a measure for the quality of the range compression, the peak-to-sidelobe ratio (PSLR) was used. Although the bandwidth of the chirp, in general, is static, the pulse sampled at reception might have a slightly reduced bandwidth depending on the time interval between two samples ($1/f_s$, $f_s =$ sampling rate) and the sampling-window start time.

The implemented correction algorithm therefore correlates the generated replica with a simulated received pulse not only for a wide range of different TEC levels but also for multiple path delays within $1/f_s$. A nearly identical path delay of the vector ensures a coherent phase and bandwidth distribution in both signals.

Fig. 2(a) shows the result of the TEC autofocus algorithm for a simulated TCR at 15 TECU and an SCR of 3 dB (raw data). The black dots mark for every time step the location of maximum correlation. The overall maximum is marked with a white dot. Variations depending on the different TEC levels and the multiple start-time positions are also visible. Fig. 2(b) shows the phase measured at the black dots in Fig. 2(a). The extent of the variations depends on the carrier frequency and sampling rate and was found to be $\approx 0.7^\circ$ for this L-band case. While Fig. 2(a) and (b) shows the results of an ensemble of 100 range lines, Fig. 2(c) shows an example of the phase error, measured for each range line, between the range-compressed phase of a TCR including noise and multiple targets (blue line) and the ideal phase distribution without noise and other scatterers present (red line). The green line is the phase error that remains after a moving average and fast Fourier transform (FFT) filtering are applied. The influence of a strong scatterer is visible at azimuth lines 200–250. A set of ten disturbing point scatterers were simulated and randomly distributed in an area of 500–1500 m (in range, azimuth around the point target) with amplitudes between 25% and 75% of the point target.

The correlation peaks when both chirps best match each other at the desired TEC level at the time

$$\begin{aligned} t_{\text{peak}} &= \frac{T_{p\_\text{iono}}}{2} + t_{\text{shift\_min\_}u/d} + \frac{2R_{\text{sat}}}{c} \\ &= \frac{T_p}{2} + \frac{K}{c} \cdot \text{TEC} \left(\frac{1}{(f_c - f_0)^2} - \frac{1}{(f_c + f_0)^2} \right) \\ &\quad + t_{\text{shift\_min\_}u/d} + \frac{2R_{\text{sat}}}{c} \end{aligned} \tag{13}$$

where R_{sat} denotes the range distance from the satellite to the target and $2R_{\text{sat}}/c$ therefore describes the round-trip delay. Equation (13) shows that the location of the target peak is independent of the chirp form. The estimation accuracy of t_{peak} depends on the length of the sampled time steps. The extraction of the peak in the range-compressed data is done using complex FFT oversampling (factor of 50) to obtain subsample accuracy. To increase the SCR, a set of 100 range lines around the TCR are focused. The range-dependent phase and the local frequency offset due to the target Doppler are removed. As the target location is sensitive to chirp-rate alterations, the range of closest approach for the TCR is calculated individually for every iteration step.

The phase distribution of the TCR over azimuth is interpolated with FFT zero padding. The range distance at closest approach is used as a reference value during range migration compensation (RMC). The range-compressed phase distribution of the simulated TCR data over azimuth was smoothed using a moving average filter and a Fourier interpolation to improve RMC. The removal of range-dependent phase relative to the closest approach (RMC) of the range line is performed by a linear phase multiplication in the frequency domain as

$$p_{\text{shifted}}(t) = FFT\left\{p_f(t)\right\} \cdot e^{j4\pi\left(\frac{f_r \Delta R}{c}\right)} \tag{14}$$

where ΔR is the range distance between the closest approach and the peak of the range-compressed TCR at the azimuth

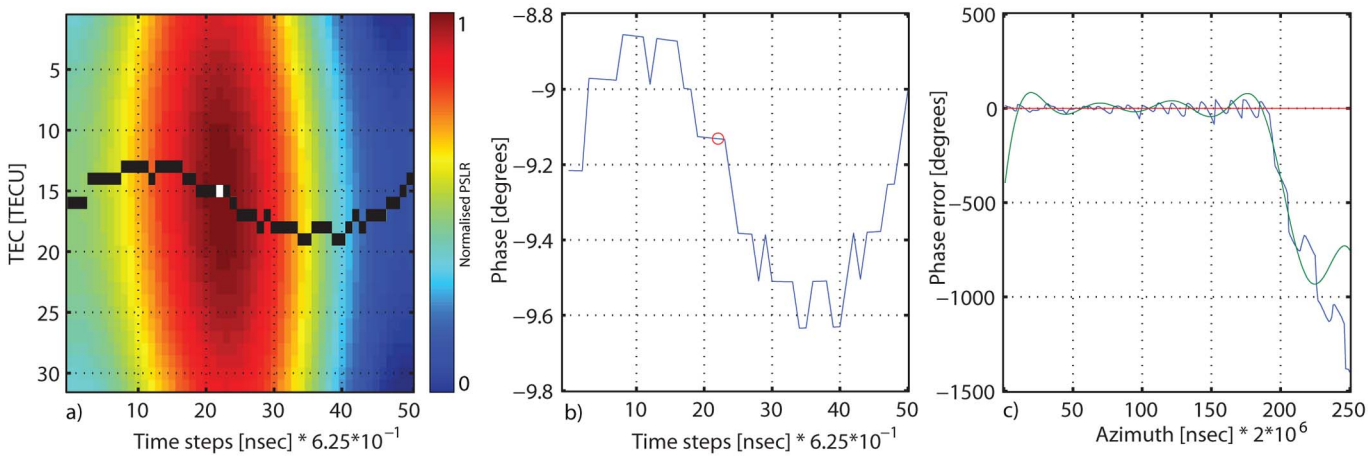

Fig. 2. (a) L-band results of TEC autofocus algorithm with detected PSLR maximum at each time step marked in black and the overall detected maximum marked as a white dot. The maximum PSLR was measured from simulations based on sets of TEC and modeled path delay used to fit the reference chirp in the matched filter. (b) Phase at maximum in correlation and (c) phase error of range-compressed target along azimuth. (Red line) Ideal case (no noise and no disturbing scatterers). (Blue line) Measured phase error. (Green line) Phase error of FFT-filtered range-compressed phase distribution. The abscissa units in range and azimuth directions are set to integer sample intervals.

TABLE II
TEC ESTIMATION USING SIMULATED L-BAND SAR DATA CONTAINING ONE TCR. ∅TEC DENOTES THE MEAN EXTRACTED TEC IN TECU OVER 50 INDEPENDENT SIMULATIONS. σ_Ω IS THE CORRESPONDING STANDARD DEVIATION OF THE TEC ESTIMATES

L-band						
SCR	**1.25 dB**		**2.5 dB**		**3 dB**	
TEC simulated	∅TEC	σ_Ω	∅TEC	σ_Ω	∅TEC	σ_Ω
5 [TECU]	8.2	7.3	9.4	4.2	4.3	3.0
15 [TECU]	16.1	7.9	16.3	6.6	15.8	6.1
25 [TECU]	22.1	7.1	22.9	6.0	23.1	4.9

TABLE III
TEC ESTIMATION USING SIMULATED P-BAND SAR DATA CONTAINING ONE TCR. ∅TEC DENOTES THE MEAN EXTRACTED TEC IN (TECU) OVER 50 INDEPENDENT SIMULATIONS. σ_Ω IS THE CORRESPONDING STANDARD DEVIATION OF THE TEC ESTIMATES

P-band						
SCR	**1.25 dB**		**2.5 dB**		**3 dB**	
TEC simulated	∅TEC	σ_Ω	∅TEC	σ_Ω	∅TEC	σ_Ω
5 [TECU]	8.4	6.5	8.3	7.5	4.4	5.9
15 [TECU]	11.3	14.2	13.4	13	10.1	13.3
25 [TECU]	24.0	12.1	23.9	8.9	21.1	9.4

position. $p_f(t)$ is the signal after removing the Doppler frequency, and f_r is the range frequency.

B. TCR Simulation Results

The feasibility of the presented technique depends mainly on the SCR within the surveyed TCR area. Simulations were carried out over a range of three noise levels under variable ionospheric conditions, including randomly distributed disturbing scatterers in the area of the examined TCR. All simulations include FR contributions appropriate to the corresponding TEC levels and a dc offset with a magnitude of the noise amplitude. The magnetic-field model necessary for FR estimation was calculated using the IGRF10 model described in Section II-B. Magnetic-field values typical at midlatitudes over the northern hemisphere were used. Each configuration was simulated 50 times to enable the approximation of the expected mean and standard deviation of the retrieved TEC levels. To increase the SCR, a limited number of 100 range lines around the range of closest approach of the TCR were focused also in azimuth.

Table II shows the L-band simulation results at 1.25-, 2.5-, and 3-dB SCR within the raw data. The TEC levels vary between 5, 15, and 25 TECU. As expected, the variability of the TEC estimates is reduced, given higher SCR or increased TEC levels. A similar behavior albeit with larger variations was observed in P-band simulations, mainly due to the comparably low number of chirp samples—summary results are shown in Table III. For the P-band simulations, the oversampling rate and the number of time steps within an interval $dt = 1/f_s$ were increased to enable a more direct comparison with the L-band simulation settings.

It becomes clear that both systems should generally be suitable for TEC estimation using strong targets. For both systems, the variability is reduced at higher TEC levels. The example simulating 5 TECU is an exception, due to the zero TEC iteration boundary. Smaller deviations were achieved when the method was applied to a larger number of selected strong scatterers within a scene. The feasibility of the autofocus technique for TEC estimation depends on the reliability requirements of the desired TEC data and improves with an increased number of chirp samples at the same carrier frequency. As seen in Table II, simulations show that the estimation of TEC seems feasible with a standard deviation of ≈6 TECU for PALSAR-type sensor configurations.

IV. POTENTIAL OF TEC ESTIMATION FROM UP- AND DOWN-CHIRP CALIBRATION BURSTS

In this section, the aim is to improve the limited accuracy expected from the previous method by adding a more direct retrieval method at the system level. In the former simulations, the initial chirp rate provided in the system specifications was

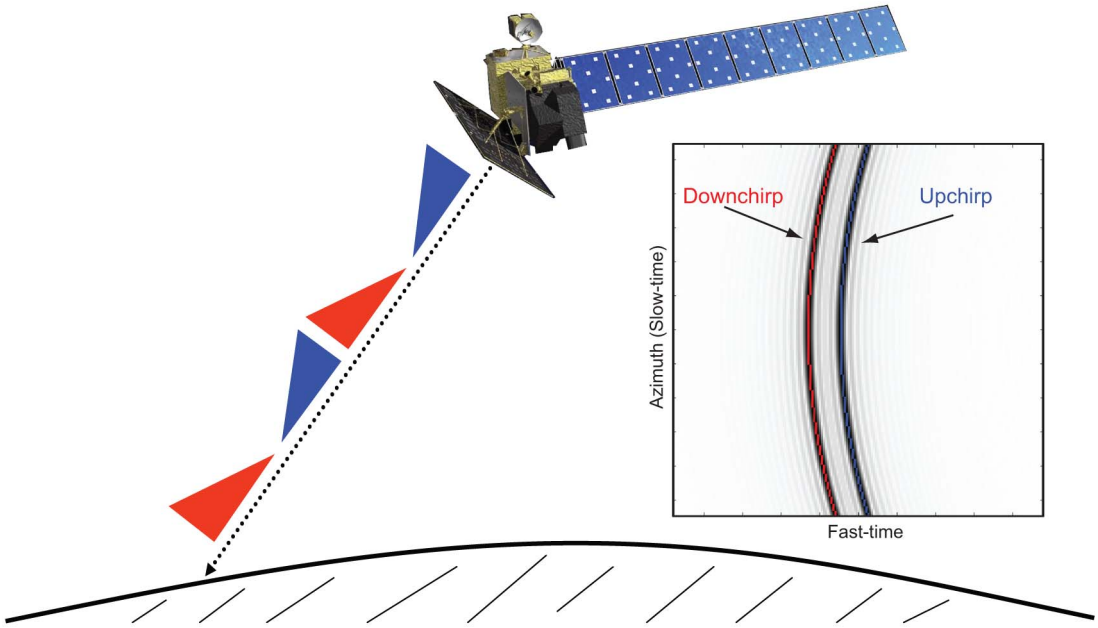

Fig. 3. Sketch of alternating chirp technique. Satellite transmits alternating up and down chirps. (On the right) Ideally range-compressed chirp pulses *dependent on the start frequency* of the chirp for a TCR under active ionospheric conditions.

iteratively adapted to derive a received pulse where both chirps match optimally. In the following, a burst of alternating up and down chirps is used to help separate the TEC from their resulting phase differences. This technique estimates TEC from alternating up and down chirps using the whole bandwidth. In contrast to earlier simulations, this method measures the differences in path delay that both chirps undergo within the same ionospheric state, making use of the ionosphere's dispersive behavior and resulting in a phase difference of the compressed target. Fig. 3 shows a sketch of an alternate chirp approach, where a satellite interleaves up and down chirps. Assuming ideal range compression, the path delays of the wave front, *dependent on the start frequencies* of the chirp, are visualized on the right. The resulting differences in path delay depend mainly on the chirp carrier frequency and the chirp bandwidth. Comparable observations might be achieved from split bandwidth arrangements without switching between up and down chirps.

The up and down chirps' starting frequencies naturally differ by the chirp bandwidth. As shown in (11) and Table I, a phase advance changes the measured chirp rate of the received pulse. This can cause a filter mismatch that is approximately equal in magnitude for both up/down chirps. While the decreased chirp rate of the down chirp causes an increased chirp length, the pulselength of the up chirp is reduced. Compared with the peak correlation location under vacuum conditions, the up chirp is shifted to precede this position (see Fig. 1).

The TEC can then be estimated using the difference between both range-compressed phase distributions, i.e., $\Delta\phi_{\mathrm{up\_down}}$ (in radians) by applying the time-delay difference evaluated between the starting frequency and the group delay of the envelope [(10) (second part) and (11)]

$$\mathrm{TEC} = \frac{\Delta\phi_{\mathrm{up\_down}} \cdot c}{4\pi f_c \cdot K} \cdot \frac{(f_c - f_0)^2 \cdot (f_c + f_0)^2}{(f_c + f_0)^2 - (f_c - f_0)^2}. \qquad (15)$$

Fig. 4(a) shows an example of the amplitude, and Fig. 4(b) shows the phase of a simulated TCR at L-band after range compression. Fig. 4(c) and (d) shows the magnified versions of Fig. 4(a) and (b).

The green line corresponds to the simulations including the path-delay differences within the chirp. To better visualize and compare the phase error caused by the filter mismatch, the blue and red lines in Fig. 4(a)–(d) show the simulation results produced when one includes only the path delay corresponding to the *start frequency* of the chirp, neglecting path-delay differences *within the chirp*. In Fig. 4(d), one sees that the down chirp is compressed to a point slightly before the up chirp. Adding the change in pulse duration shifts the down-chirp half of the change in pulselength toward the up chirp and vice versa. Both pulses overlap at the position of the expected group delay (green line). As the pulses are already in baseband, this shift has only a small effect on the phase of the chirps [seen from Fig. 4(d)]. Table IV shows the estimated phase differences between the mean up- and down-chirp phases of a focused TCR. The results were additionally calculated for a typical X-band sensor configuration (TerraSAR-X, $B = 300$ MHz). As expected, sensitivity is higher in the P-band configuration. However, due to the higher chirp bandwidth, sensitivity at X-band remains high enough to theoretically be able to extract the ionospheric state at 1-TECU levels. Technical realization would require further investigation.

V. Discussion and Conclusion

With the European Space Agency (ESA)'s candidate Earth explorer BIOMASS carrying a P-band SAR as its payload, the need to estimate the ionospheric state before an acquisition is imperative. One suitable method could be by sending a burst of quad-polarized pulses that enable the measurement of FR

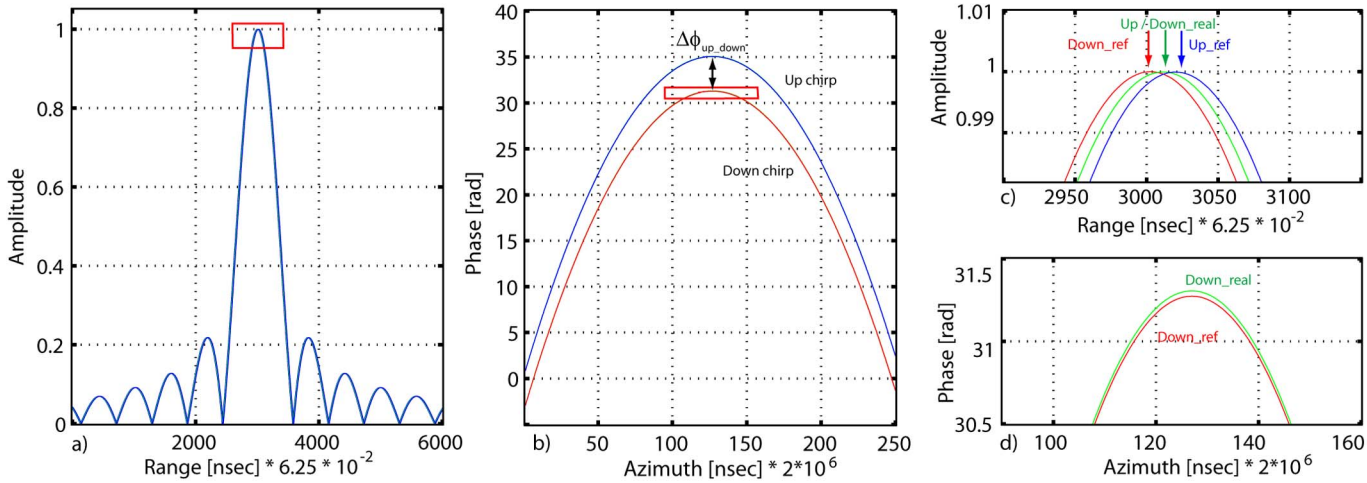

Fig. 4. (a) L-band range-compressed up and down chirps after passing through an ionosphere modeled at a state of 15 TECU along the signal path (of a TCR). The red line simulates a down chirp, and the blue line simulates an up chirp. The blue and red lines were simulated considering only a constant ionospheric path delay based on the starting frequency of the chirp (ref = rigid shift without frequency dependence). The green line also considers the frequency-dependent path delays within the chirp (real). (a) Range-compressed pulses. (b) Phase distribution of the chirp pulses. (c) and (d) Close-ups of the plot areas indicated in (a) and (b). The abscissa units in range and azimuth directions are set to integer sample intervals.

TABLE IV
SENSITIVITY OF P-, L-, AND X-BAND SENSORS USING THE UP- AND DOWN-CHIRP TECHNIQUE AT 1, 5, AND 15 TECU. K_{NORM} ESTIMATED AT L-BAND FOR 1 TECU WAS USED FOR NORMALIZATION

System:	**P-band**	**L-band**	**X-band**
f_c [GHz]	0.435	1.27	9.65
B [MHz]	6	28	300
$K_{\mathrm{NORM}} \cdot \frac{B}{f_c^2}$	1.83	1	0.19
TEC [TECU]	$\Delta\phi_{\mathrm{up\_down}}$	$\Delta\phi_{\mathrm{up\_down}}$	$\Delta\phi_{\mathrm{up\_down}}$
1	61.3°	33.6°	6.2°
5	306.7°	168.0°	31.2°
15	920.3°	503.9°	93.5°

along the signal path. This paper shows two alternative methods that make use of the frequency-dependent path delay that a chirp undergoes while passing through the ionosphere. These techniques estimate the local TEC along the signal path and can be single-polarized measurements. The estimation of FR from TEC measurements additionally requires knowledge of the magnetic field.

The first method shown uses an autofocus technique that optimizes the reference chirp to be used for range compression, maximizing the PSLR where the ionospheric effects on the recovered chirp's shape are best modeled. The estimation of TEC using this method requires a strong contrast within the scene—limiting applicability in areas such as forests. Simulations show that the extraction of TEC from one strong TCR appears feasible when the SCR (of the raw data) is above 2.5 dB. The feasibility of the autofocus technique for estimating TEC depends mainly on the resolution requirements of the desired TEC data and the number of chirp samples. Simulations of L-band sensor configurations showed that the estimation of TEC seems feasible with a standard deviation of 6 TECU. Additional simulations at higher TEC levels showed improved accuracy, but still cannot compare with TEC results from the dense GPS networks over North America or Europe. One advantage of the method is that the measurements from the radar data estimate the TEC directly along the observation path with directly relevant spatial and temporal resolutions. Improvements to SCR could be made by combining the information from a set of strong scatterers within a scene. As this method would be much more time consuming and less suitable for operational use, the systematic alternate up/down pulse methodology would be favored where possible.

Phase differences in the L-band simulations were as high as 30°/TECU. TEC estimation at 1-TECU levels then becomes possible without requiring specific reference targets. The delimitation of the achievable accuracies is currently being investigated. No hardware changes on the satellite module should be necessary [28]. A second matched filter as well as pulse generation could be added/modified through software revisions.

Consideration of this technique should include as an option recording the whole scene using the alternating chirp method. As the shapes of the pulses are different, future applications might consider increasing the PRF, as pulses could overlap more closely [26]. For calibration, one could also use a quad-polarized calibration burst. The measurement of TEC and FR in a calibration burst additionally enables the estimation of the geomagnetic field. As scintillations mainly come from electron-density irregularities in the E- and F-region and one can reasonably assume a linearly varying geomagnetic field within the space of an acquisition, the FR data from a quad-polarized acquisition could be transferred straightforwardly into a corresponding high-resolution TEC map.

In addition to dc offset, disturbing targets, and varying noise levels, the simulations enable the modeling of the frequency-dependent FR. As FR changes the orientation angle of the radar wave, a single-polarized antenna would see a very small frequency-dependent amplitude modulation of the chirp signal, not expected to significantly reduce the sensitivity of the TEC estimation techniques. The simulated dc offset was removed by subtracting the mean without noticeably corrupting the results.

A first test and validation of the alternating chirp technique could be realized by building a transponder that switches between up- and down-chirp replicas. Sensitivity tests using simulations show that TerraSAR-X acquisitions would also be suitable for analysis.

ACKNOWLEDGMENT

The authors would like to thank B. Rommen and B. Rastburg-Arbesser of ESA European Space Research and Technology Centre (ESTEC) for their scientific input and financial support during the initial stages of the software development.

REFERENCES

[1] E. J. M. Rignot, R. Zimmermann, and J. J. van Zyl, "Spaceborne applications of P band imaging radars for measuring forest biomass," *IEEE Trans. Geosci. Remote Sens.*, vol. 33, no. 5, pp. 1162–1169, Sep. 1995.

[2] M. Jehle, M. Rüegg, D. Small, E. Meier, and D. Nüesch, "Estimation of ionospheric TEC and Faraday rotation for L-band SAR," *Proc. SPIE*, vol. 5979, pp. 252–260, Oct. 2005.

[3] Z.-W. Xu, J. Wu, and Z.-S. Wu, "A survey of ionospheric effects on space-based radar," *Waves Random Media*, vol. 14, no. 12, pp. 189–272, Apr. 2004.

[4] Z.-W. Xu, J. Wu, and Z.-S. Wu, "Potential effects of the Ionosphere on space-based SAR imaging," *IEEE Trans. Antennas Propag.*, vol. 56, no. 7, pp. 1968–1975, Jul. 2008.

[5] F. Meyer, R. Bamler, N. Jakowski, and T. Fritz, "The potential of low-frequency SAR systems for mapping ionospheric TEC distributions," *IEEE Geosci. Remote Sens. Lett.*, vol. 3, no. 4, pp. 560–564, Oct. 2006.

[6] S. H. Bickel and R. H. T. Bates, "Effects of magneto-ionic propagation on the polarization scattering matrix," *Proc. IEEE*, vol. 53, no. 8, pp. 1089–1091, Aug. 1965.

[7] E. J. M. Rignot, "Effect of Faraday rotation on L-band interferometric and polarimetric synthetic-aperture radar data," *IEEE Trans. Geosci. Remote Sens.*, vol. 38, no. 1, pp. 383–390, Jan. 2000.

[8] W. B. Gail, "Effect of Faraday rotation on polarimetric SAR," *IEEE Trans. Aerosp. Electron. Syst.*, vol. 34, no. 1, pp. 301–307, Jan. 1998.

[9] P. A. Wright, S. Quegan, N. S. Wheadon, and C. D. Hall, "Faraday rotation effects on L-band spaceborne data," *IEEE Trans. Geosci. Remote Sens.*, vol. 41, no. 12, pp. 2735–2744, Dec. 2003.

[10] R.-Y. Qi and Y.-Q. Jin, "Analysis of the effects of Faraday rotation on spaceborne polarimetric SAR observations at P-band," *IEEE Trans. Geosci. Remote Sens.*, vol. 45, no. 5, pp. 1115–1122, May 2007.

[11] A. Freeman and S. S. Saatchi, "On the detection of Faraday rotation in linearly polarized L-band SAR backscatter signatures," *IEEE Trans. Geosci. Remote Sens.*, vol. 42, no. 8, pp. 1607–1616, Aug. 2006.

[12] A. Freeman, "Calibration of linearly polarized polarimetric SAR data subject to Faraday rotation," *IEEE Trans. Geosci. Remote Sens.*, vol. 42, no. 8, pp. 1617–1624, Aug. 2004.

[13] M. Jehle, M. Rüegg, L. Zuberbühler, D. Small, and E. Meier, "Measurement of ionospheric Faraday rotation in simulated and real spaceborne SAR data," *IEEE Trans. Geosci. Remote Sens.*, vol. 47, no. 5, pp. 1512–1523, May 2009.

[14] W. B. Gail, "A simplified calibration technique for polarimetric radars," in *Proc. IGARSS*, Tokyo, Japan, Aug. 1993, vol. 2, pp. 377–379.

[15] R. Touzi and M. Shimada, "On the use of symmetric scatterers for calibration and validation of PALSAR polarimetric modes," in *Proc. IGARSS*, Anchorage, AK, Sep. 2004, vol. 3, pp. 1835–1837.

[16] D. H. Hoekman and M. J. Quiriones, "Land cover type and biomass classification using AirSAR data for evaluation of monitoring scenarios in the Colombian Amazon," *IEEE Trans. Geosci. Remote Sens.*, vol. 38, no. 2, pp. 685–696, Mar. 2000.

[17] B. Hallberg, G. Smith, A. Olofsson, and L. M. H. Ulander, "Performance simulation of spaceborne P-band SAR for global biomass retrieval," in *Proc. IGARSS*, Anchorage, AK, Sep. 2004, vol. 1, pp. 503–506.

[18] J. Nicoll, F. Meyer, and M. Jehle, "Prediction and detection of Faraday rotation in ALOS PALSAR data," in *Proc. IGARSS*, Barcelona, Spain, 2007, pp. 5210–5213.

[19] F. J. Meyer and J. B. Nicoll, "Prediction, detection, and correction of Faraday rotation in full-polarimetric L-band SAR data," *IEEE Trans. Geosci. Remote Sens.*, vol. 46, no. 10, pp. 3076–3086, Oct. 2008.

[20] P. C. Dubois-Fernandez, J.-C. Souyris, S. Angelliaume, and F. Garestier, "The compact polarimetry alternative for spaceborne SAR at low frequency," *IEEE Trans. Geosci. Remote Sens.*, vol. 46, no. 10, pp. 3208–3222, Oct. 2008.

[21] S. Schaer, *Mapping and Predicting the Earth's Ionosphere Using the Global Positioning System*. Zürich, Switzerland: Inst. Geodäsie Photogram., Eidg. Technische Hochschule Zürich, 1999.

[22] U. Hugentobler, M. Meindl, G. Beutler, H. Bock, R. Dach, A. Jäggi, C. Urschl, L. Mervart, M. Rothacher, S. Schaer, E. Brockmann, D. Ineichen, A. Wiget, U. Wild, G. Weber, H. Habrich, and C. Boucher, CODE IGS analysis center technical report 2003/2004, Astron. Inst., Univ. Bern, Bern, Switzerland. [Online]. Available: http://www.aiub.unibe.ch/content/research/gnss/publications/

[23] S. Macmillan and S. Maus, "International geomagnetic reference field—The tenth generation," *Earth Planets Space*, vol. 57, no. 12, pp. 1135–1140, Dec. 2005.

[24] R. F. Hanssen, *Radar Interferometry*. Norwell, MA: Kluwer, 2001.

[25] I. G. Cumming and F. H. Wong, *Digital Processing of Synthetic Aperture Radar Data, Algorithms and Implementation*. Boston, MA: Artech House, 2005.

[26] G. H. Millman and C. D. Bell, "Ionospheric dispersion of an FM electromagnetic pulse," *IEEE Trans. Antennas Propag.*, vol. AP-19, no. 1, pp. 152–155, Jan. 1971.

[27] P. H. Eichel, D. C. Ghiglia, and C. V. Jakowatz, "Speckle processing method for synthetic-aperture-radar phase correction," *Opt. Lett.*, vol. 14, no. 1, pp. 1–3, Jan. 1989.

[28] U. Stein and M. Younis, "Suppression of range ambiguities in synthetic aperture radar systems," in *Proc. EUROCON*, Sep. 2003, vol. 2, pp. 417–421.

Michael Jehle (S'07) received the Dipl.Ing. degree in electrical engineering from the University of Karlsruhe, Karlsruhe, Germany, in 2002 and the Ph.D. degree from the University of Zurich, Zurich, Switzerland, in 2009.

After that, he was a Scientist in projects for the Institute for Very High Frequency Technology and Electronics, University of Karlsruhe, and with the Klinikum für Sportorthopädie Abteilung Biomechanik, Albert-Ludwigs-Universität Freiburg, Freiburg, Germany. He is currently a Research Assistant with the Remote Sensing Laboratories, Department of Geography, University of Zurich. His research interests include electromagnetic-wave propagation in the atmosphere, signal processing, and synthetic aperture radar systems.

Othmar Frey (S'04–M'08) received the M.Sc. degree in geomatic engineering from the Swiss Federal Institute of Technology (ETH) Zurich, Zurich, Switzerland, in 2002.

Since 2002, he has been with the Remote Sensing Laboratories, Department of Geography, University of Zurich, Zurich, as a Research Associate, where he has worked on a geometric error budget analysis for TerraSAR-X data products and on atmospheric effects in synthetic aperture radar (SAR) data until 2003/2004 and where he is currently working in the field of SAR signal processing. His research interests include SAR focusing algorithms in general and SAR tomography and other advanced SAR imaging modes in particular. He has developed and implemented SAR signal processing software that allows for end-to-end data processing of advanced imaging modes, such as airborne multibaseline SAR and SAR data acquisitions from nonlinear flight tracks.

Mr. Frey has contributed to invited sessions on SAR tomography at the European Conference on Synthetic Aperture Radar (EUSAR) 2008 and at the International Geoscience and Remote Sensing Symposium 2008, where he was a Session Cochair. He is a Reviewer for the IEEE TRANSACTIONS ON GEOSCIENCE AND REMOTE SENSING and the IEEE GEOSCIENCE AND REMOTE SENSING LETTERS. He was the recipient of the ETH medal for an outstanding master thesis.

David Small (S'85–M'98) received the B.A.Sc. degree in systems design engineering from the University of Waterloo, Waterloo, ON, Canada, in 1988, the M.A.Sc. degree in electrical engineering from the University of British Columbia, Vancouver, BC, Canada, in 1991, and the Ph.D. degree from the University of Zurich, Zurich, Switzerland, in 1998. In his Ph.D. thesis, he developed a processing chain for generating digital elevation models from repeat-pass ERS data.

He works on SAR geometric and radiometric calibration issues as a member of the European Space Agency's SAR Quality Working Group. Together with Erich Meier, he leads the SAR group at the Remote Sensing Laboratories, Department of Geography, University of Zurich. His research is in the fields of synthetic aperture radar (SAR) polarimetry and interferometry, as well as geometric and radiometric calibrations of SAR imagery.

Erich Meier (M'09) received the M.Sc. degree in geography and the Ph.D. (Hons.) degree in remote sensing from the University of Zurich, Zurich, Switzerland, in 1982 and 1989, respectively.

From 1979 to 1982, he was a Research Assistant with the Remote Sensing Section and, from 1982 to 1983, with the GIS Laboratory, Department of Geography, University of Zurich. From 1983 to 2006, he was a Research Scientist with the Remote Sensing Laboratories (RSL), Department of Geography, University of Zurich, where he is currently the Research Section Head involved in teaching as well as in research in digital image processing, software development for computer graphics, and radiometric and geometric calibrations of SAR and optical imagery. Since 2000, he has been the Head of the SARLab, a research group within RSL. The main research interests of this group are the development of new focusing algorithms for SAR data from UHF to millimeter wave, interferometry, polarimetry, and moving target indication algorithms, as well as calibration and validation activities for spaceborne and airborne systems. He is responsible for the research strategies as well as the organization of the team. He is a Consultant on behalf of several national and international organizations and private companies.